PAPER

Modulation doping of transition metal dichalcogenide/oxide heterostructures†

Kang Xu, Yi Wang, Yuda Zhao and Yang Chai*

Control of carrier type and carrier density provides a way to tune the physical properties of two-dimensional (2D) semiconductors. Modulation doping of heterostructures can effectively inject carriers into or extract carriers from the 2D semiconductors, and eliminate the adverse effect from the ionized dopants. Here we first investigate the layer-dependent negative trion PL of 2D MoS_2, and further construct heterostructures with transition metal dichalcogenides (TMDs) and transition metal oxides (TMOs). By choosing the oxide with different charge neutrality levels (CNLs), we demonstrate effective electron injection into MoS_2 by TiO_2 doping, and electron extraction from MoS_2 by MoO_3 doping. Photoluminescence (PL) spectra and electrical characterization show that thicker MoS_2 flakes are more easily n-doped by TiO_2, while thinner MoS_2 flakes are more easily p-doped by MoO_3. Our experimental results are in good agreement with theoretical calculations. The modulation doping with TMO is compatible with conventional Si processing and highly air-stable. This method can also be extended for the controllable doping of other 2D materials.

Introduction

Two-dimensional (2D) layered transition metal dichalcogenides (TMDs) are of great research interest because of their unique electronic, optical and optoelectronic properties.[1–5] The modulation of carrier density in the TMDs provides a way to change their physical properties in a controllable manner. For typical TMD materials, the pristine carrier type is predominated by their intrinsic characteristics. For example, pristine MoS_2 is of the n-type while WSe_2 shows p-type or ambipolar characteristics (the carrier type of WSe_2 is dependent on its thickness).[2,6–8] Controllable injection and extraction of electrons/holes are important for effective n- and p-doping of TMDs, which are crucial for building complementary logic circuits in the future. On the other hand, the interaction between carriers and excitons enables an additional path for the PL modulation of 2D layered materials. Controlling the carrier type and density through modulation doping provides a way to switch between exciton- and trion-dominant PL and tune the PL intensity of 2D materials.[9]

Various methods have been developed to dope 2D layered TMDs,[10] including substitutional doping during growth,[11] ion implantation,[12] plasma treating,[13] *etc.* Although these doping methods have been demonstrated to be effective, they inevitably result in the distortion of TMD crystal structures, introduce

Department of Applied Physics, The Hong Kong Polytechnic University, Hung Hom, Kowloon, Hong Kong, P. R. China. E-mail: ychai@polyu.edu.hk

† Electronic supplementary information (ESI) available. See DOI: 10.1039/c6tc04640a

ionized impurity scattering canters, and degrade the charge mobility. Modulation doping has been widely used in III–V compound heterojunction superlattices to eliminate the influence of ionized impurity scattering.[14–16] In the heterojunction device, the ionized dopants and electrons are confined to two different adjacent layers. As a result, both the mobility and carrier concentration are well maintained. A variety of dopants have been studied for the surface charge transfer to TMDs, including gas molecules,[17] organics,[18] metal particles[19] and oxides.[2,20] Among these kinds of dopants, oxide is one of the promising species due to its stability in ambience and compatibility with conventional Si processing technology.

In this work, we deposit transition metal oxide (TMO) on top of 2D MoS_2 to form a heterojunction device. We choose TiO_2 with a high charge neutrality level (CNL) and MoO_3 with a low CNL for injecting and extracting electrons, respectively. Our optical and electrical characterization, together with density functional theory (DFT) calculations, shows that TiO_2 and MoO_3 deposition gives rise to effective n-doping and p-doping, respectively. In addition, we also reveal layer-dependent negative trion photoluminescence (PL) and doping effects in 2D layered MoS_2. This approach opens up a way to control the characteristics of PL and the electrical transport of 2D layered materials.

Results and discussion

Layer-dependent negative trion PL of 2D MoS_2

Because of the extremely strong Coulomb interaction in ultrathin 2D MoS_2, optically generated excitons (*i.e.*, electron–hole pairs)

376 | *J. Mater. Chem. C*, 2017, 5, 376–381

This journal is © The Royal Society of Chemistry 2017

and trions (*i.e.*, charged excitons) can exist stably at room temperature.[21] Electrons are excited to the conducting band, leaving holes in the valence band. Electrons and holes are then bound together by Coulomb interactions to form neutrally charged excitons (electron–hole pairs). Due to the Coulomb attraction between the hole in an exciton and a third electron, the formation process of exciton to trion is energy favourable.[22] Trions are formed in the presence of residual free charges. Fig. 1(a) shows the PL spectra of a 3L MoS_2 as an example. Two pronounced peaks around 1.87 eV and 2.05 eV are clearly observed, defined as the A exciton peak and the B exciton peak, respectively. As schematically depicted in the inset, the A exciton has originated from the radiative recombination of the excited electrons in the conduction band minimum (CBM) with the holes in the valence band minimum (VBM); and the B exciton has originated from the radiative recombination of the excited electrons in the CBM with the lower branch of the split VBM.[23] The A exciton of ultrathin MoS_2 can be further devolved into a neutron exciton (X) peak around 1.9 eV and a negative trion (X^-) peak around 1.85 eV.[21]

Fig. 1(b) shows the PL spectra of MoS_2 evolved with the layer number from 1L to 4L. The PL spectra of over 60 MoS_2 flakes were collected and are summarized in Fig. 1(c) and (d). Fig. 1(c) shows the layer-dependent spectral weight of the X^- peak in the whole A exciton peak, which rapidly decreases from 90% in the 1L MoS_2 to 30% in the 3L–5L MoS_2. There are two possible reasons accounting for the layer-dependent characteristic of the spectral weight of the X^- peak. First, electrons in MoS_2 originated from donor states introduced by surface sulfur vacancies,[24–27] which are expected to become less prominent with the increase of body thickness. Second, when the thickness of MoS_2 increases, the dielectric screening of MoS_2 increases,[28,29] which attenuates the Coulomb interaction[30] and reduces the binding energy of trions. With the decrease of binding energy,

trion systems are less stable and can be easily decomposed into excitons. Fig. 1(d) shows the photon energy of X and X^- peaks as a function of MoS_2 thickness. The PL peaks exhibit a clear red-shift with an increase of MoS_2 body thickness due to the decreased bandgap. In the inset of Fig. 1(d), we present the layer-dependent energy difference (binding energy of the negative trion from the exciton) between X and X^- peaks. This binding energy decreases with the increase of MoS_2 thickness.

Layer-dependent n-doping of MoS_2 by TiO_2

Fig. 2 shows the PL spectra of 1L–4L MoS_2 before and after TiO_2 deposition. After 6 nm thick Atomic Layer Deposition (ALD) TiO_2 doping, we observe the characteristics of layer-dependent PL. The thicker MoS_2 sample has a smaller X^- spectral weight before the TiO_2 deposition, which is consistent with our previous discussions; while the X^- spectral weight increases more after the TiO_2 deposition. These changes in PL spectra are ascribed to the injection of electrons from TiO_2 into MoS_2, where the electron density in MoS_2 is increased by TiO_2 doping.

To rule out the possibility that this PL change has originated from in-plain lattice strain due to oxide deposition on the surface, we also present the corresponding Raman spectra before and after doping in Fig. S1 (ESI†). As widely reported by previous research studies, the in-plane lattice strain induces the split of the E_{2g}^1 peak and the blue-shift of both E_{2g}^1 and A_{1g} peaks.[31] However, from our Raman spectra, we observe no such Raman spectral change. Thus, it is suggested that the interlayer coupling between the TiO_2 layer and the MoS_2 surface is very weak, and this weak interaction induces negligible lattice strain to MoS_2. So the PL spectral change has not originated from the lattice strain. To confirm this speculation, we further deposited 30 nm thick TiO_2 onto 1L–3L MoS_2. The Raman and PL spectra are shown in Fig. S2 (ESI†). We still observe a more significant increase of the X^- spectral weight in thicker MoS_2 and a negligible shift of Raman peaks. It is noteworthy that the attenuation of Raman intensity after the doping is possibly due to the block of light of the 30 nm thick TiO_2 layer. On the other hand, the change of the dielectric environment introduced by TiO_2
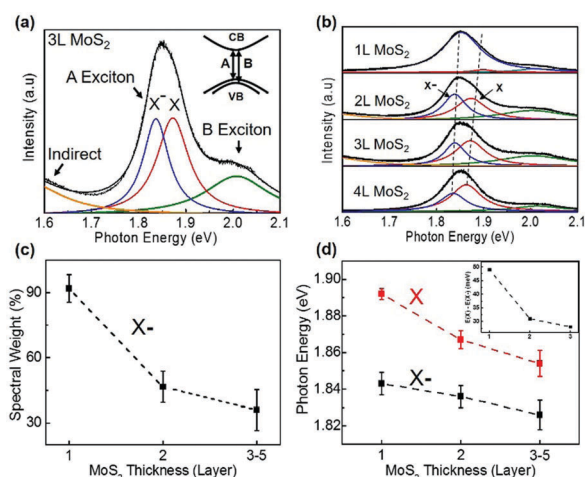

Fig. 1 PL analysis of ultrathin MoS_2 flakes. (a) PL spectrum of 3L MoS_2. The inset shows the radiative recombination path of A and B excitons, respectively. (b) PL spectra of 1L–4L MoS_2. (c) Layer-dependent spectral weight of the X^- peak. (d) Layer-dependent photon energy of the X peak and the X^- peak in the MoS_2 samples from 1L to 5L. The inset shows the layer-dependent energy difference between the X peak and the X^- peak.
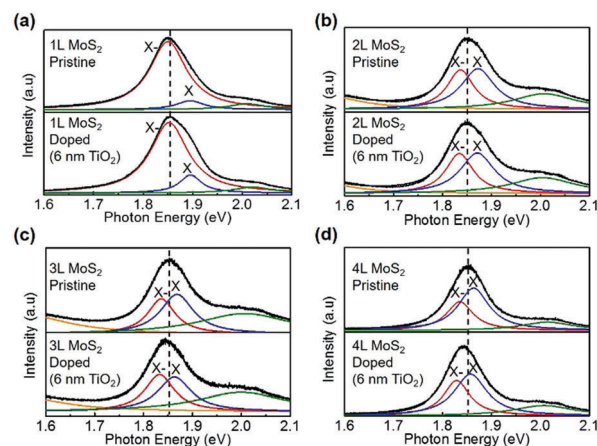

Fig. 2 PL spectra of ultrathin MoS_2 flakes before and after depositing 6 nm thick TiO_2. The thicknesses of MoS_2 samples are (a) 1L, (b) 2L, (c) 3L and (d) 4L.

deposition plays an important role in the change of the PL spectra of MoS_2. In both cases (6 nm thick and 30 nm thick TiO_2), the A exciton peak is found to be red-shifted after the TiO_2 deposition, which is more obvious in the case of 30 nm thick TiO_2 deposition. This is because the bandgap of MoS_2 is decreased in the environment with a higher dielectric constant (the dielectric constant of TiO_2 is ~80).[30] Furthermore, from the point of view of enhanced dielectric screening in MoS_2 due to the deposition of the TiO_2 layer, the Coulomb interaction in MoS_2 is attenuated (similar to the effect of increasing MoS_2 body thickness). The attenuated Coulomb interaction decreases the binding energy of the negative trion, thus decreasing the stability of the trion system and the PL intensity of the X^- peak. However, in our experiments, the PL intensity of the X^- peak is obviously increased after the TiO_2 doping. Therefore, the increase of the X^- peak PL is due to the increase of electron density in MoS_2, which originated from the n-doping effect by TiO_2.

To further confirm and quantify the n-doping effect, we fabricated a back-gated MoS_2 field effect transistor (FET) and doped it with 6 nm thick ALD TiO_2. Fig. 3(a) depicts the cross-sectional schematic of a back-gated MoS_2 FET with its channel covered by TMO. Fig. 3(b) shows the transfer curve of a 5L MoS_2 FET before (black line) and after (red line) the 6 nm thick TiO_2 doping. The pristine device shows typical n-type behaviour, consistent with previous reports.[1,32] After n-doping, the ON current (I_{ON}) is increased by a factor of 4 at V_{bg} = 50 V. Fig. 3(c) and (d) show the output curves of the same device before and after doping, respectively. Again, I_{ON} at V_{bg} = 50 V is found to be amplified about 5 times. It is noteworthy that the device retains its semiconducting characteristics after the doping, indicating that the n-doping effect is non-degenerate. Furthermore, we can extract 2D sheet carrier density (n_{2D}) and field-effect mobility (μ_{FE}) according to eqn (1) and (2), where L and W are the channel length and the channel width, respectively, and C_{ox} is the capacitance of the gated oxide (i.e., 1.16×10^{-8} F cm^{-2}

for 300 nm thick SiO_2 in this study).[1] The extracted n_{2D} before doping is 1.17×10^{12} cm^{-2}, which is consistent with previous reports,[32–35] while the extracted n_{2D} after the doping is 1.95×10^{12} cm^{-2}. This doping level (0.78×10^{12} cm^{-2}) is comparable with other doping methods (i.e., 2×10^{11} cm^{-2} for OTS-doped WSe_2,[36] 4.6×10^{11} cm^{-2} for MEA-doped MoS_2,[37] -2×10^{11} cm^{-2} for FDT-doped MoS_2,[34] and 1×10^{13} cm^{-2} for TiO_x-doped graphene).[37] The μ_{FE} and n_{2D} are extracted at V_{bg} = 30 V. Although the doping effect is independent of the back gate voltage, sufficient gate voltage is required to turn on the channel of the device. It is noteworthy that in these devices, the charges are free carriers without the formation of excitons or trions. Because there is no external input to excite electrons to the conduction band and the lifetimes of excitons and trions are very short, in the order of picoseconds,[38,39]

$$\mu_{FE} = \frac{d}{dV_g} I_{ds} \times \frac{L}{W \times C_{ox} \times V_{ds}} \qquad (1)$$

$$n_{2D} = \frac{I_{ds} \times L}{W \times \mu_{FE} \times V_{ds}} \qquad (2)$$

To further support our findings, DFT calculations were utilized to simulate the doping effect. The anatase phase TiO_2 structure was used in this simulation since it is a stable phase at a relatively low temperature.[20] Fig. 4(a) and (b) show the atomic and orbital projected density of states of pristine $1H$-MoS_2, $1H$-MoS_2 in the TiO_2-doped MoS_2 system, anatase TiO_2, and anatase TiO_2 in the TiO_2-doped MoS_2 system. The bandgap of pristine $1H$-MoS_2 is calculated to be ~1.86 eV. And both the conduction band minimum (CBM) and the valence band maximum (VBM) of MoS_2 are populated by the 4d orbital of the Mo atom, which are highly hybridized with the 3p orbital of the S atom.[20] After the TiO_2 doping, the Fermi level of 1L MoS_2 is up-shifted approximately 0.76 eV towards the CBM, indicating
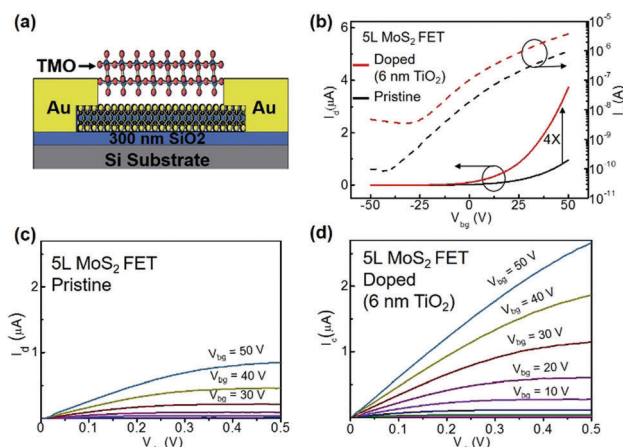

Fig. 3 Electrical characterization of a MoS_2 FET for n-doping by TiO_2. (a) Cross-sectional schematic of a TMO doped MoS_2 FET. (b) Transfer curve of a 5L MoS_2 FET before (black line) and after (red line) being doped by 6 nm thick TiO_2. (c) Output curves of the FET before doping; (d) output curves of the FET after doping.
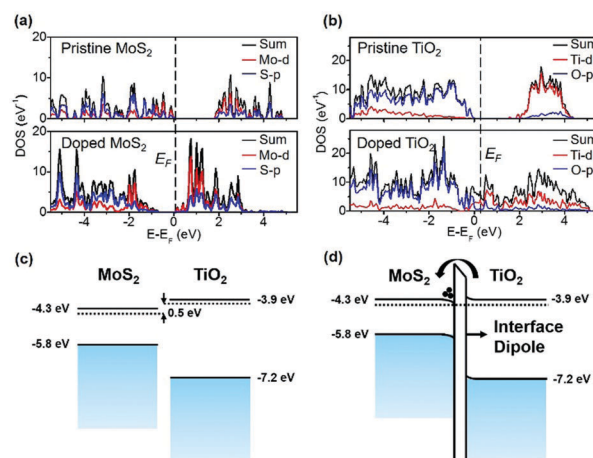

Fig. 4 DFT simulation results of the n-doping process and band structures of MoS_2 and TiO_2. (a) DOS of 1L $1H$-MoS_2 before (upper panel) and after doping (lower panel). (b) DOS of anatase TiO_2 before (upper panel) and after doping MoS_2 (lower panel). (c) Band alignment of 1L MoS_2 and TiO_2 before doping. (d) Band alignment of 1L MoS_2 and TiO_2 after doping. The dashed lines denote the CNL.

the n-doping effect. Also, the bandgap of MoS_2 is obviously shrunken, which is due to the enhanced dielectric screening introduced by TiO_2 deposition. From Fig. 4(b), we observe a significant change in the DOS of TiO_2 after the n-doping. Compared with the pristine state, the presence of the Ti-5d level in the conduction band is dramatically decreased. This change indicates that electrons are mainly transferred from the Ti-5d level of TiO_2 to MoS_2, leaving the Ti-5d level anti-bonding. Similar findings regarding the simulation of the TiO_2 doping process can be found in the work of N. Kaushik et al.[40]

Fig. 4(c) shows the schematic band structures of 1L MoS_2 versus anatase TiO_2. The CBM and CNL of MoS_2 are about 0.5 eV lower than those of TiO_2. Driven by this energy difference, electrons in the CB of TiO_2 flows into the CB of MoS_2, until an interface dipole pointing from MoS_2 to TiO_2 is built up (Fig. 4(d)) and then the doping process reaches its balance state. As widely acknowledged, electrons in ultrathin MoS_2 flakes have originated from surface sulfur vacancies. It is reasonable to expect that this surface effect has a smaller influence on the electronic structure of thicker MoS_2 samples. The CNL of MoS_2 thin flakes lowers when the thickness of MoS_2 increases. Considering the fact that the bandgap of MoS_2 decreases with the increase of body thickness, the CNL of thicker MoS_2 samples quickly lowers down. For thicker MoS_2 samples, the energy difference between its CNL and that of TiO_2 enlarges, thus the n-doping effect is more obvious.

Layer-dependent p-doping of MoS_2 by MoO_3

MoO_3 is one type of TMOs with a relatively low CNL. We choose it for p-doping MoS_2. Fig. 5 shows the PL spectra of 1L and 3L MoS_2 before and after 6 nm thick MoO_3 doping. In both cases, a significant decrease of the X^- peak spectral weight is observed. The corresponding Raman spectra of these samples are shown in Fig. S3 (ESI†). No obvious shift in the positions of Raman peaks is observed, suggesting that the interlayer coupling between the MoO_3 layer and the MoS_2 surface is also very small. Also, it is noteworthy that the dielectric constant of MoO_3 is small (~ 5.5). Therefore, it has a negligible influence on the PL spectra of MoS_2.

Electrical characterization of MoS_2 FETs is used to further quantify the p-doping effect. Fig. 6(a) is the transfer curve of a 5L MoS_2 FET before and after p-doping. After the p-doping, the I_{ON} at V_{bg} = 50 V is decreased 5 times and the threshold voltage (V_{th}) is increased by ~ 24 V. The extracted n_{2D} values are 2.3×10^{12} cm^{-2} before the doping and 1.7×10^{12} cm^{-2} after the p-doping. The electron density in MoS_2 is depleted by about 0.6×10^{12} cm^{-2},

Fig. 6 Electrical characterization of a MoS_2 FET for p-doping by MoO_3. (a) Transfer curve of a 5L MoS_2 FET before (black line) and after (red line) 6 nm thick MoO_3 doping. (b) Output curves of the device before doping. (c) Output curves of the device after 6 nm thick MoO_3 doping. (d) Extracted μ_{FE} (left axis) and n_{2D} (right axis) of three MoS_2 devices before (black line) and after (red line) 6 nm thick MoO_3 doping.

which is comparable to the doping level of 6 nm thick TiO_2 (0.78×10^{12} cm^{-2}). The corresponding output curves of the device are illustrated in Fig. 6(b) (before doping) and Fig. 6(c) (after doping). As expected, we observe a decrease of I_{ON} in the positive gate range (0–50 V). The gate voltage required to turn on the channel (V_{ON}) is clearly increased from 20 V to 30 V. The n_{2D} and μ_{FE} values of MoS_2 devices before and after the p-doping are summarized in Fig. 6(d). For thicker MoS_2 samples, the depleted electron density is smaller.

This layer dependence can also be ascribed to the decrease of the CNL of MoS_2 with the increase of body thickness, as discussed in the case of n-doping by TiO_2. Due to the reduced carrier density, electrons undergo a stronger scattering effect from the interface defects, which will significantly reduce the carrier mobility.

DFT calculation results of this p-doping process are shown in Fig. 7. In Fig. 7(a), the Fermi level of 1L MoS_2 is moved down towards the VB, demonstrating the p-doping effect. The DOS of MoO_3 in Fig. 7(b) shows that the population of the Mo-4d orbital is increased after the doping, indicating that electrons are transferred from the Mo-4d orbital in MoS_2 to the Mo-4d orbital in MoO_3. Fig. 7(c) illustrates the schematic band structure of 1L MoS_2 versus MoO_3. The CNL of MoS_2 is 2.2 eV higher than that of MoO_3. Due to this energy difference, electrons in the CB of MoS_2 are extracted to the CB of MoO_3 until an interface dipole is built up (Fig. 7(d)). When the CNL of MoS_2 is lowered down by increasing the body thickness, the energy difference between it and the CNL of MoO_3 is decreased, thus leading to a decreased p-doping effect.

Experimental

Fabrication of MoS_2 FETs

MoS_2 crystals were purchased from a commercial producer (2D semiconductors). Mechanically exfoliated MoS_2 thin flakes
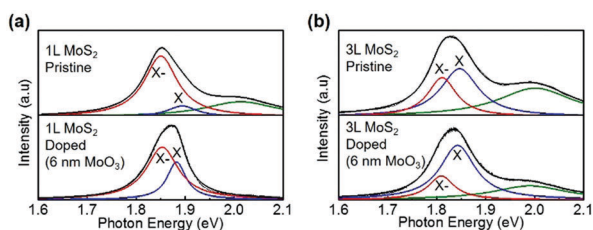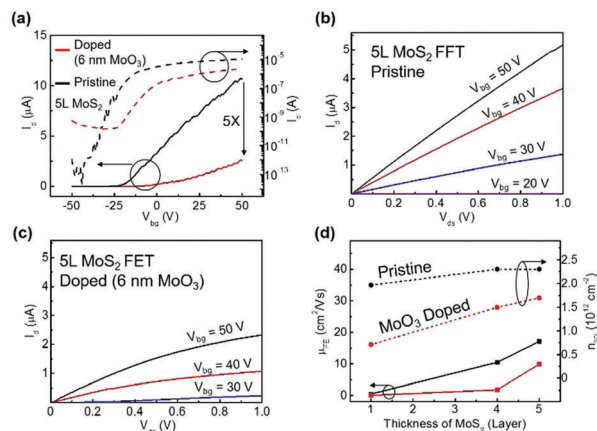

Fig. 5 PL spectra of ultrathin MoS_2 flakes before and after being doped by 6 nm thick MoO_3. The thicknesses of MoS_2 samples are (a) 1L and (b) 3L.

This journal is © The Royal Society of Chemistry 2017

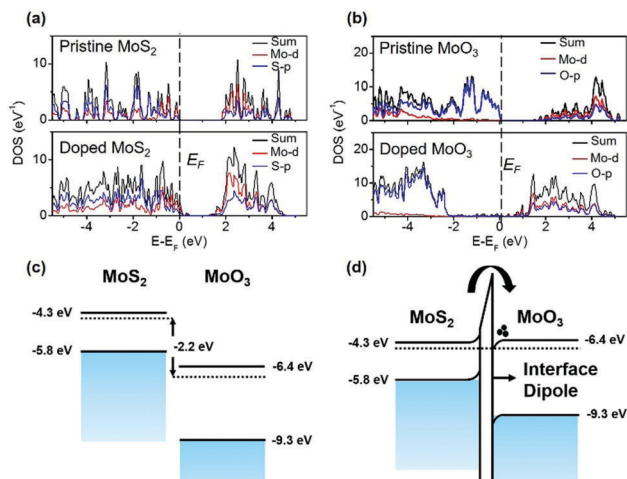*J. Mater. Chem. C*, 2017, **5**, 376–381 | **379**

Fig. 7 DFT simulation results of the p-doping process and band structures of MoS$_2$ and MoO$_3$. (a) DOS of 1L 1H-MoS$_2$ before (upper panel) and after doping (lower panel). (b) DOS of pristine MoO$_3$ before (upper panel) and after doping MoS$_2$ (lower panel). (c) Band alignment of 1L MoS$_2$ and MoO$_3$ before doping. (d) Band alignment of 1L MoS$_2$ and MoO$_3$ after doping. The dashed lines denote the CNL.

were used to fabricate FETs. Target substrates (300 nm thick SiO$_2$/Si wafer) were contacted with Scotch tape and then bathed in Acetone or Isopropyl Alcohol (IPA) at 60 °C to remove organic residues. Ultrathin flakes (<10 nm) of MoS$_2$ were identified using an optical microscope. The conventional photo-lithography process was performed, followed by metal deposition and lift-off processes. Metal electrodes (i.e., Ti/Au) were deposited using an electron-beam evaporator at a rate of ∼0.7 Å s^{-1}. Electrical characteristics of the FETs were measured using a Keithley 4200-SCS Semiconductor Parameter Analyser.

Deposition of TiO$_2$ and MoO$_3$ oxide layers

TiO$_2$ oxide layers were deposited on MoS$_2$ using ALD at 150 °C. The sources were tetrakis(dimethylamino)titanium (TDMAT) and H$_2$O. The deposition rate was ∼0.47 Å cycle^{-1}. A thermal evaporator was used to deposit MoO$_3$ oxide layers. The source was MoO$_3$ powder. The deposition rate was around 1 Å s^{-1}. The oxide layers are continuous and have small surface roughness.

DFT simulations of the doping process

DFT calculations were conducted using Quantum ESPRESSO to simulate the charge transfer process between oxide and TMDs. The ion cores were described using projector-augmented wave sets and scalar-relativistic pseudopotentials. The generalized gradient approximation Perdew–Burke–Ernzerhof (PBE) exchange–correlation was selected as the pseudopotential functional type. $2 \times 1 \times 1$ monolayer MoO$_3$ was constituted on the top of $2 \times 1 \times 1$ 1H-MoS$_2$ along the (001) direction, and $2 \times 1 \times 1$ TiO$_2$ was constituted on the $2 \times 1 \times 1$ 1H-MoS$_2$ along the (001) direction. Each supercell contains a 40 Å vacuum region in the z-axis to prevent the effects from the neighbouring slabs. The convergence threshold values on the total energy and force were 10^{-6} and 10^{-3}, respectively. The kinetic energy cut-off for wave functions was 50 Ry, and the kinetic energy cut-off for charge density and potential was 200 Ry.

Conclusions

In summary, we investigate the layer dependence of n- and p-doping of MoS$_2$ by TMO. TiO$_2$ and MoO$_3$ are used for the n- and p-doping of MoS$_2$, respectively. PL and electrical characterization show that thicker MoS$_2$ samples are more easily n-doped by TiO$_2$; while thinner MoS$_2$ samples are more easily p-doped by MoO$_3$. Furthermore, the doping levels of 6 nm thick TiO$_2$ and MoO$_3$ are extracted to be 0.78×10^{12} cm^{-2} and 0.6×10^{12} cm^{-2}, respectively. Our experiments characterized the doping effects and doping levels of the two mostly used oxide dopants (TiO$_2$ and MoO$_3$) and shed light on optimizing the doping strategy of TMDs by oxide layers.

Acknowledgements

References

1 B. Radisavljevic, A. Radenovic, J. Brivio, I. V. Giacometti and A. Kis, Nat. Nanotechnol., 2011, 6, 147–150.

2 C. Zhou, Y. Zhao, S. Raju, Y. Wang, Z. Lin, M. Chan and Y. Chai, Adv. Funct. Mater., 2016, 26, 4223.

3 Y. Zhao, J. Qiao, P. Yu, Z. Hu, Z. Lin, S. P. Lau, Z. Liu, W. Ji and Y. Chai, Adv. Mater., 2016, 28, 2399.

4 Z. Lin, Y. Zhao, C. Zhou, R. Zhong, X. Wang, Y. H. Tsang and Y. Chai, Sci. Rep., 2015, 5, 18596.

5 C. Zhou, X. Wang, S. Raju, Z. Lin, D. Villaroman, B. Huang, H. L.-W. Chan, M. Chan and Y. Chai, Nanoscale, 2015, 7, 8695–8700.

6 W. Liu, J. Kang, D. Sarkar, Y. Khatami, D. Jena and K. Banerjee, Nano Lett., 2013, 13, 1983–1990.

7 J.-K. Huang, J. Pu, C.-L. Hsu, M.-H. Chiu, Z.-Y. Juang, Y.-H. Chang, W.-H. Chang, Y. Iwasa, T. Takenobu and L.-J. Li, ACS Nano, 2013, 8, 923–930.

8 Y. Zhang, J. Ye, Y. Matsuhashi and Y. Iwasa, Nano Lett., 2012, 12, 1136–1140.

9 S. Mouri, Y. Miyauchi and K. Matsuda, Nano Lett., 2013, 13, 5944–5948.

10 Y. Zhao, K. Xu, F. Pan, C. Zhou, F. Zhou and Y. Chai, Adv. Funct. Mater., 2016, DOI: 10.1002/adfm.201603484.

11 J. Suh, T.-E. Park, D.-Y. Lin, D. Fu, J. Park, H. J. Jung, Y. Chen, C. Ko, C. Jang and Y. Sun, Nano Lett., 2014, 14, 6976–6982.

12 A. Nipane, D. Karmakar, N. Kaushik, S. Karande and S. Lodha, ACS Nano, 2016, 10, 2128–2137.

13 M. Chen, H. Nam, S. Wi, L. Ji, X. Ren, L. Bian, S. Lu and X. Liang, Appl. Phys. Lett., 2013, 103, 142110.

14 R. Dingle, H. Störmer, A. Gossard and W. Wiegmann, Appl. Phys. Lett., 1978, 33, 665–667.

380 | J. Mater. Chem. C, 2017, 5, 376–381

This journal is © The Royal Society of Chemistry 2017

15 R. People, J. Bean, D. Lang, A. Sergent, H. Störmer, K. Wecht, R. Lynch and K. Baldwin, *Appl. Phys. Lett.*, 1984, **45**, 1231–1233.

16 T. Mimura, S. Hiyamizu, T. Fujii and K. Nanbu, *Jpn. J. Appl. Phys.*, 1980, **19**, L225.

17 P. Zhao, D. Kiriya, A. Azcatl, C. Zhang, M. Tosun, Y.-S. Liu, M. Hettick, J. S. Kang, S. McDonnell, S. KC, J. Guo, K. Cho, R. M. Wallace and A. Javey, *ACS Nano*, 2014, **8**, 10808–10814.

18 D. Kiriya, M. Tosun, P. Zhao, J. S. Kang and A. Javey, *J. Am. Chem. Soc.*, 2014, **136**, 7853–7856.

19 C.-H. Chen, C.-L. Wu, J. Pu, M.-H. Chiu, P. Kumar, T. Takenobu and L.-J. Li, *2D Mater.*, 2014, **1**, 034001.

20 N. Kaushik, D. Karmakar, A. Nipane, S. Karande and S. Lodha, *ACS Appl. Mater. Interfaces*, 2015, **8**, 256–263.

21 K. F. Mak, K. He, C. Lee, G. H. Lee, J. Hone, T. F. Heinz and J. Shan, *Nat. Mater.*, 2013, **12**, 207–211.

22 A. Singh, G. Moody, K. Tran, M. E. Scott, V. Overbeck and G. Berghäuser, *Phys. Rev. B*, 2016, **93**(4), 041401.

23 G. Berghäuser and E. Malic, *Phys. Rev. B: Condens. Matter Mater. Phys.*, 2014, **89**, 125309.

24 D. Liu, Y. Guo, L. Fang and J. Robertson, *Appl. Phys. Lett.*, 2013, **103**, 183113.

25 S. Kim, M. S. Choi, D. Qu, C. H. Ra, X. Liu, M. Kim, Y. J. Song and W. J. Yoo, *2D Mater.*, 2016, **3**, 035002.

26 E. Rotunno, F. Fabbri, E. Cinquanta, D. Kaplan, M. Longo, L. Lazzarini, A. Molle, V. Swaminathan and G. Salviati, *2D Mater.*, 2016, **3**, 025024.

27 A. Splendiani, L. Sun, Y. Zhang, T. Li, J. Kim, C.-Y. Chim, G. Galli and F. Wang, *Nano Lett.*, 2010, **10**, 1271–1275.

28 X. Chen, Z. Wu, S. Xu, L. Wang, R. Huang, Y. Han, W. Ye, W. Xiong, T. Han and G. Long, 2014, arXiv:1407.5365.

29 T. Cheiwchanchamnangij and W. R. Lambrecht, *Phys. Rev. B: Condens. Matter Mater. Phys.*, 2012, **85**, 205302.

30 Y. Lin, X. Ling, L. Yu, S. Huang, A. L. Hsu, Y.-H. Lee, J. Kong, M. S. Dresselhaus and T. S. Palacios, *Nano Lett.*, 2014, **14**, 5569–5576.

31 L. Yang, X. Cui, J. Zhang, K. Wang, M. Shen, S. Zeng, S. A. Dayeh, L. Feng and B. Xiang, *Sci. Rep.*, 2014, **4**, 5649.

32 S. Das, H.-Y. Chen, A. V. Penumatcha and J. Appenzeller, *Nano Lett.*, 2012, **13**, 100–105.

33 H.-Y. Park, M.-H. Lim, J. Jeon, G. Yoo, D.-H. Kang, S. K. Jang, M. H. Jeon, Y. Lee, J. H. Cho and G. Y. Yeom, *ACS Nano*, 2015, **9**, 2368–2376.

34 D. M. Sim, M. Kim, S. Yim, M.-J. Choi, J. Choi, S. Yoo and Y. S. Jung, *ACS Nano*, 2015, **9**, 12115–12123.

35 B. Radisavljevic and A. Kis, *Nat. Mater.*, 2013, **12**, 815–820.

36 D.-H. Kang, J. Shim, S. K. Jang, J. Jeon, M. H. Jeon, G. Y. Yeom, W.-S. Jung, Y. H. Jang, S. Lee and J.-H. Park, *ACS Nano*, 2015, **9**, 1099–1107.

37 P. H. Ho, C. H. Chen, F. Y. Shih, Y. R. Chang, S. S. Li, W. H. Wang, M. C. Shih, W. T. Chen, Y. P. Chiu and M. K. Li, *Adv. Mater.*, 2015, **27**, 7809–7815.

38 Q. Wang, S. Ge, X. Li, J. Qiu, Y. Ji and J. Feng, *ACS Nano*, 2013, **7**(12), 11087–11093.

39 D. Lagarde, L. Bouet, X. Marie, C. R. Zhu, B. L. Liu, T. Amand, P. H. Tan and B. Urbaszek, *Phys. Rev. Lett.*, 2014, **112**(4), 047401.

40 N. Kaushik, D. Karmakar, A. Nipane, S. Karande and S. Lodha, *ACS Appl. Mater. Interfaces*, 2015, **8**(1), 256–263.

This journal is © The Royal Society of Chemistry 2017

J. Mater. Chem. C, 2017, **5**, 376–381 | 381